Supplementary Information for

Unlocking the Loading Limit in Single-Atom Photocatalysts via Defect-Induced Metal Trapping

Laihao Liu[1], Yucong Huang[1], Xiaocang Han[2], Chuyue Lu[1], Jingjing Xiong[1],* Yuqing Qiu[1], Guanwu Lian[1], Fanrun Jin[1], Wenguang Tu[1], Xiaoxu Zhao[2], Zhigang Zou[1], Zhongxin Chen[1,]*

* Correspondence and requests for materials should be addressed to J. Xiong (jingjxiong@cuhk.edu.cn) and Z. Chen (chenzhongxin@cuhk.edu.cn)

[1] Guangdong Basic Research Center of Excellence for Aggregate Science, School of Science and Engineering, The Chinese University of Hong Kong, Shenzhen, 518172, China.

[2] School of Materials Science and Engineering, Peking University, Beijing, 100871, China.

Supplementary Methods

Materials. Analytical grade reagents were used directly without further purification. Indium chloride ($InCl_3$), thioacetamide (TAA), nickel chloride hexahydrate ($NiCl_2$, 99.0%), and cobalt (II) chloride hydrate ($CoCl_2$, 99.0%) were bought from Shanghai Macklin Biochemical Technology Co., Ltd. Zinc acetate dihydrate ($Zn(CH_3COO)_2 \cdot 2H_2O$) and ethanol (AR) were bought from Shanghai Aladdin Biochemical Technology Co., Ltd. Carbon paper (CP, TGP-H-120) was obtained from Suzhou Sinero Technology Co., Ltd. 2-Propanol (IPA, AR) was bought from Shanghai Titan Scientific Co., Ltd. Sulfuric acid (AR) was purchased from Guangdong Guangshi Regent Technology Co., Ltd. Deionized water (DI water, ≥18 MΩ) was obtained from ultrapure water system.

Synthesis of $ZnIn_2S_4$. In a representative experiment, $InCl_3$ (1 mmol), TAA (4 mmol), and $Zn(CH_3COO)_2 \cdot 2H_2O$ (0.5 mmol) were dissolved in 50 mL of DI water and stirred at room temperature for 30 min. The solution was transferred to a 100 mL stainless steel autoclave and maintained at 180 °C for 18 hours. After cooling to room temperature, the yellowish powder ($ZnIn_2S_4$ or ZIS) was separated by centrifugation, followed by washing with DI water and ethanol three times and drying at 60 °C overnight.

Preparation of CP-ZIS. 400 mg of ZIS was dispersed in 40 mL of ethanol and sonicated for 40 minutes to obtain a homogeneous dispersion. The dispersion was then sprayed uniformly onto a piece of carbon paper (2 × 10 cm^2) several times to achieve a mass loading of 15 mg cm^{-2} and dried in an oven overnight. The ZIS-coated carbon paper (CP-ZIS) was then cut into 2 × 2 cm^2 for further use.

Synthesis of Sv-ZIS. As-prepared CP-ZIS was electrochemically desulfurized in the H-cell using a two-electrode configuration. The anode was CP-ZIS (2 × 2 cm^2), the cathode was a Pt electrode, and the electrolyte was 0.5 M H_2SO_4. The electrochemical desulfurization of CP-ZIS was conducted for varying periods at different voltages to prepare Sv-ZIS with varying degrees of desulfurization (vacancy). The optimal sample by electrochemical desulfurization at -3.5 V for 10 minutes was denoted as Sv-ZIS.

Synthesis of Sv-ZIS-M SACs. In a typical synthesis of monometallic Sv-ZIS-Co, as-prepared Sv-ZIS was held in place with a clamping device and immersed in 60 mL of IPA containing 10 mM $CoCl_2$ in a photo-reactor with a quartz window. Single-atom deposition of Co was carried out under various light intensities (suns), wavelengths, and deposition periods. The material obtained by an optimal deposition at a light intensity of 10 suns for 1.5 hours was defined as Sv-ZIS-Co. The preparation of Sv-ZIS-Ni was identical to Sv-ZIS-Co, except that 10 mM $CoCl_2$ was replaced by 10 mM $NiCl_2$. For bimetallic Sv-ZIS-CoNi, a higher concentration of $CoCl_2$ and $NiCl_2$ (20 mM) was adopted in ethylene glycol to obtain a similar loading to monometallic variants. Monometallic samples were photodeposited in IPA, while bimetallic Sv-ZIS-CoNi was deposited in ethylene glycol (EG). This is because of a higher solubility of metal salts in EG and a better tolerance to photothermal load to prevent excessive solvent evaporation during 10-sun irradiation

Material characterization. The following equipment was used: STEM (Titan Cubed Themis G2300, 200 kV), HRTEM (JEOL JEM-F200, 200 kV), X-ray diffraction (XRD) patterns were collected on a Rigaku Smartlab Powder X-ray diffractometer

using Cu K_α radiation (40 kV, 40 mA) at room temperature, XPS measurements were carried out in a Thermo Scientific Nexsa system with an Al K_α ($h\nu$ = 1,486.7 eV) as the excitation source for XPS, and the XPS data was calibrated by C 1s spectrum (binding energy is 284.8 eV). Electron paramagnetic resonance (EPR) measurement was conducted on a Bruker EMX PLUS spectrometer with a 9.054 GHz magnetic field. Raman spectra were obtained using a LabRAM HR Evolution Raman spectrometer with an excitation wavelength of 325 nm to analyze the composition. The light absorption property was investigated using the PERSEE T700 UV-vis spectrophotometer, with barium sulfate as a standard reference. The sulfide test kit, using methylene blue colorimetry, was purchased from the Hach company (product #: 181732, Hach method 8131).

Degree of desulfurization by UV-vis. To prevent the escape of H_2S, the S-containing extracted solution was immediately neutralized with NaOH to a pH of 7, producing Na_2S and Na_2SO_4. A certain amount of solution was collected and diluted to the detection range (typically 50 to 100 times dilution). Then, the diluted solution was determined by UV-vis spectra using a commercial sulfur test kit. The concentration was determined by external calibration curves using a series of standard Na_2S solutions from 0.01 to 0.5 mg mL^{-1}.

Turnover frequency (TOF). In photocatalytic water splitting (*e.g.*, $ZnIn_2S_4$ systems), the Turnover Frequency (TOF) is a critical metric for evaluating the intrinsic activity of catalysts, representing the number of reaction cycles per active site per unit time. Below is the professional calculation method:

$$TOF\left(h^{-1}\right)=\frac{\text{Number of } H_2 \text{ molecules produced}}{\text{Number of active sites} \times \text{Reaction time}}$$

Apparent quantum yield (AQY). The AQY was measured under the same reaction conditions as the photocatalytic test, except that the incident light was supplied by a 300W Xe lamp equipped with specific band-pass filters to achieve the desired monochromatic incident wavelengths (375, 420, 475, 520, and 600 nm). AQY was roughly calculated based on the following equation:

$$AQY=\frac{\text{The number of reacted electrods}}{\text{The number of incident photons}}\times 100\%$$

$$=\frac{4\times \text{the number of } H_2 \text{ molecules}}{\text{The number of incident photons}}\times 100\%$$

$$=\frac{4\times \text{the number of } H_2 \text{ molecules}}{N}\times 100\%$$

Density functional theory (DFT) calculations. Density functional theory (DFT) simulations (1, 2) were performed using the Vienna *ab initio* Simulation Package (VASP) with a plane-wave basis set and the projector augmented-wave (PAW) method. (3, 4) To model the exchange-correlation effects, the generalized gradient approximation (GGA) with the Perdew-Burke-Ernzerhof (PBE) functional(5) was employed, supplemented by Grimme's DFT-D3 dispersion(6) correction to account for van der Waals interactions. A plane-wave energy cutoff of 450 eV was applied throughout the calculations. A 4 × 4 × 1 supercell of the $ZnIn_2S_4$ (001) surface was constructed for the simulations. To mimic bulk-like conditions, the atoms in the bottom three atomic layers were fixed during structural relaxation, while a vacuum layer of 15 Å was introduced along the *c*-axis to eliminate spurious periodic interactions. Brillouin-

zone integrations were conducted using a gamma-centered *k*-point grid. Structural optimizations proceeded until the maximum force on any atom fell below 0.02 eV $Å^{-1}$, with an energy convergence threshold of 10^{-5} eV. Transition states were identified via the climbing-image nudged elastic band (CI-NEB) method and the dimer algorithm, ensuring residual forces remained under 0.05 eV $Å^{-1}$.

The Gibbs free energy (ΔG) was evaluated using the thermodynamic relation:

$$\Delta G = \Delta E + \Delta ZPE - T\Delta S$$

where ΔE represents the total energy from DFT, ΔZPE denotes the zero-point energy correction, and $T\Delta S$ accounts for temperature-dependent entropic effects.

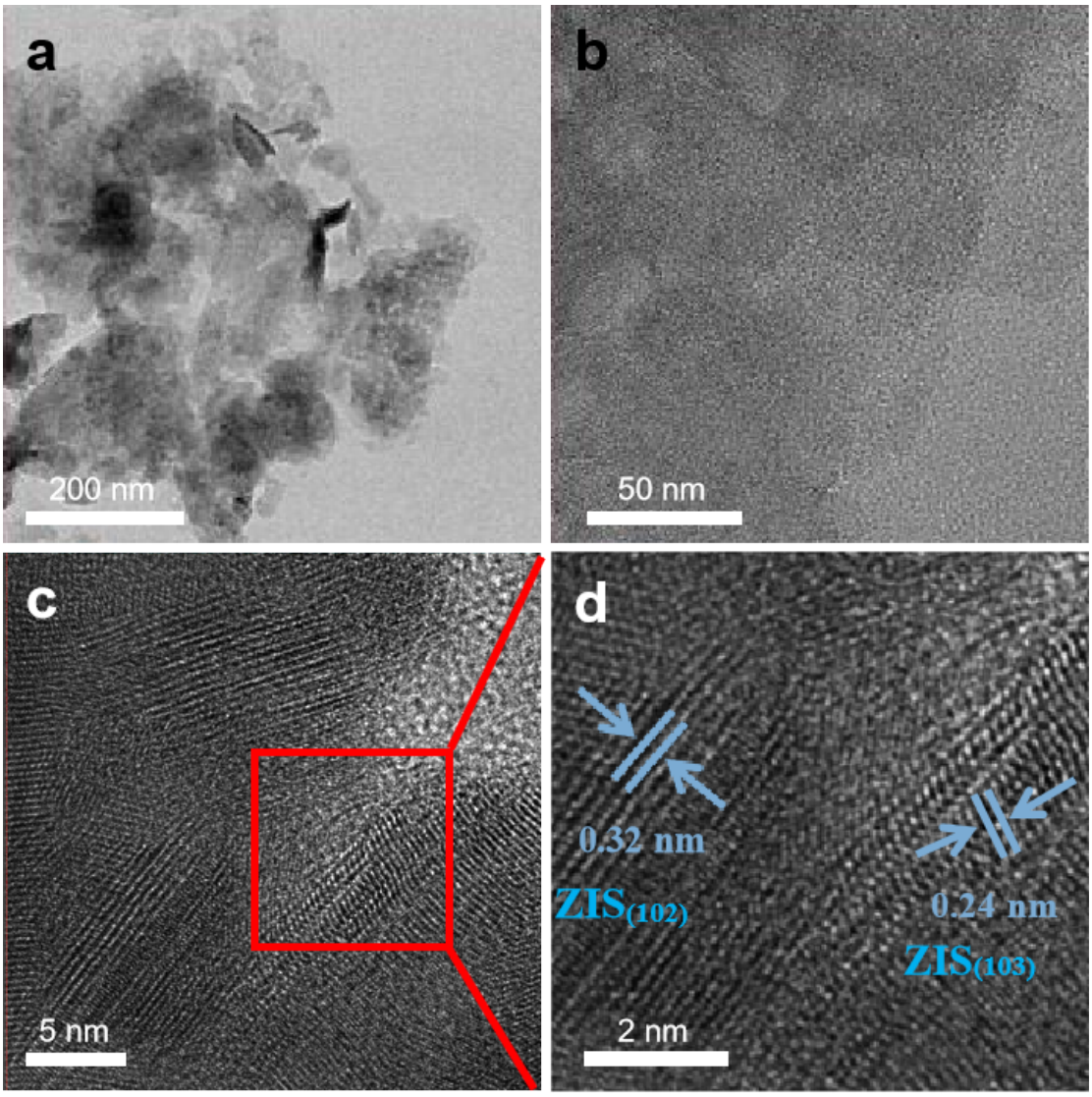

Figure S1. (a-c) The TEM images of ZIS at various magnifications; (d) an enlarged image of the red box area in (c). The lattice spacings of 0.32 nm and 0.24 nm in **Figure S1D** represent the (102) and (103) planes of ZIS, respectively.

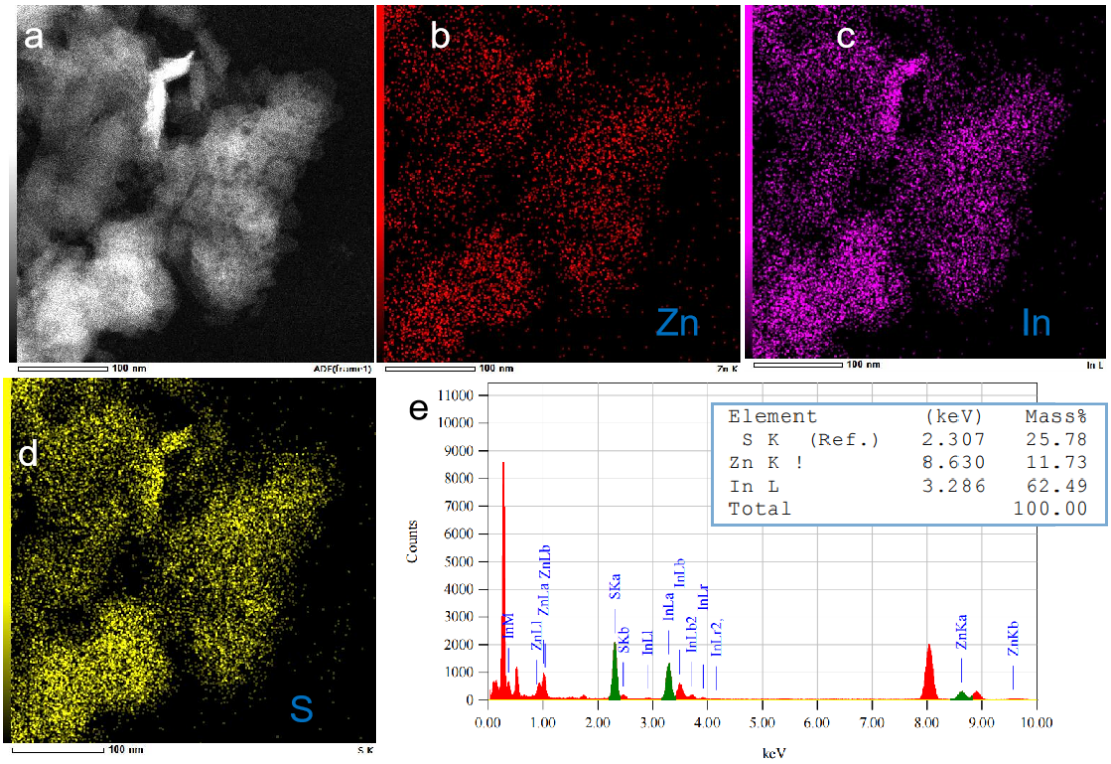

Figure S2. (a-d) EDS mapping and (e) the corresponding energy spectrum of ZIS.

As shown in **Figure S1**, pristine ZIS shows a characteristic multi-layered nanosheet morphology in high-resolution transmission electron microscopy (HRTEM) images. Clear lattice fringes can be observed in pristine ZIS, whose lattice spacings of 0.32 and 0.24 nm are assignable to the (102) and (103) crystal planes (JCPDS: 65-2023).(7-9) The corresponding energy-dispersive X-ray spectroscopy (EDS) mappings in **Figure S2** confirm the stoichiometric ratio of $ZnIn_2S_4$ and uniform distribution of Zn, In, and S elements across the sample.

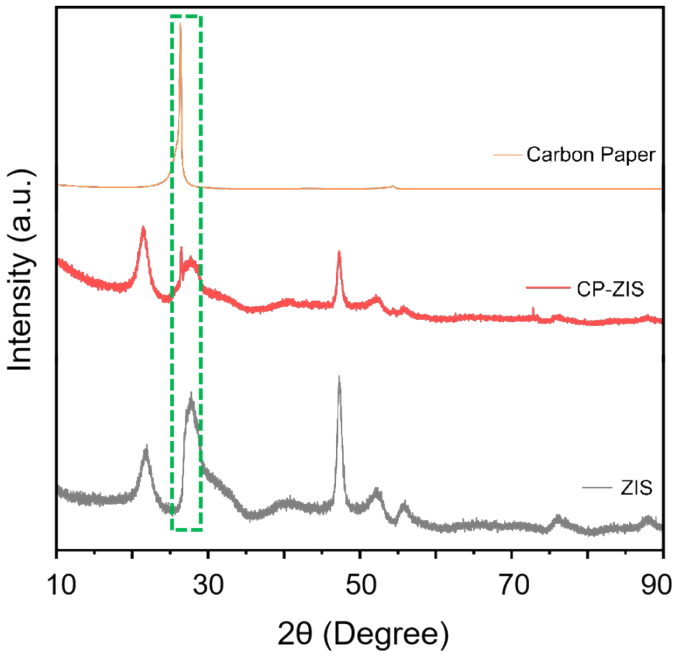

Figure S3. The XRD patterns of ZIS, CP-ZIS and carbon paper (CP). The XRD pattern in Figure S3 reveals typical peaks at 21.6°, 27.7°, 39.8°, 47.2°, 52.4°, and 76.4°, corresponding to the (006), (102), (108), (110), (116), and (213) crystal planes of ZIS, respectively.(10) An additional peak associated with the carbon paper at around 27° could be observed and will not be detailed further.

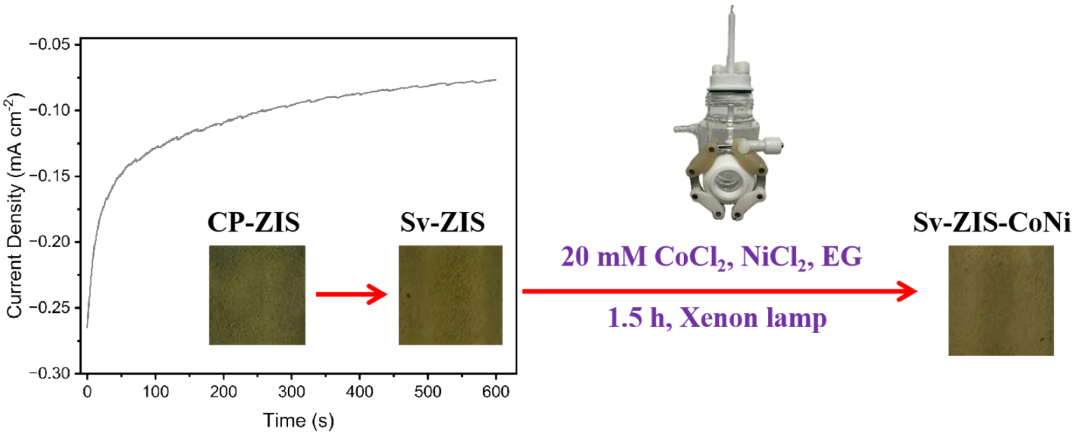

Figure S4. Electrochemical desulfurization and subsequent photodeposition of Co and Ni single atoms to synthesize bimetallic Sv-ZIS-CoNi.

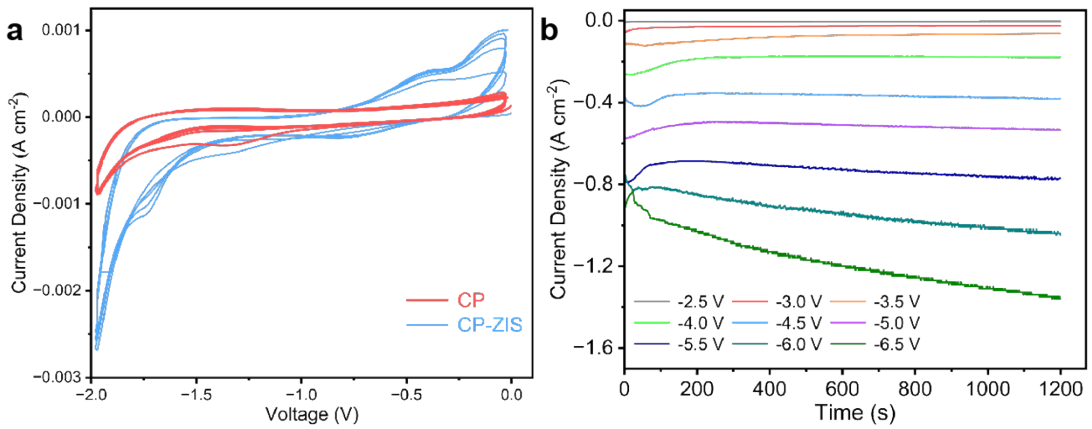

Figure S5. (a) CV curves of blank CP and CP-ZIS in an electrolyte of 0.5 M H_2SO_4, showing a prominent peak at ~ -1.5 V from the desulfurization of ZIS; (b) I-t curves at various voltages to prepare Sv-ZIS with different desulfurization degrees.

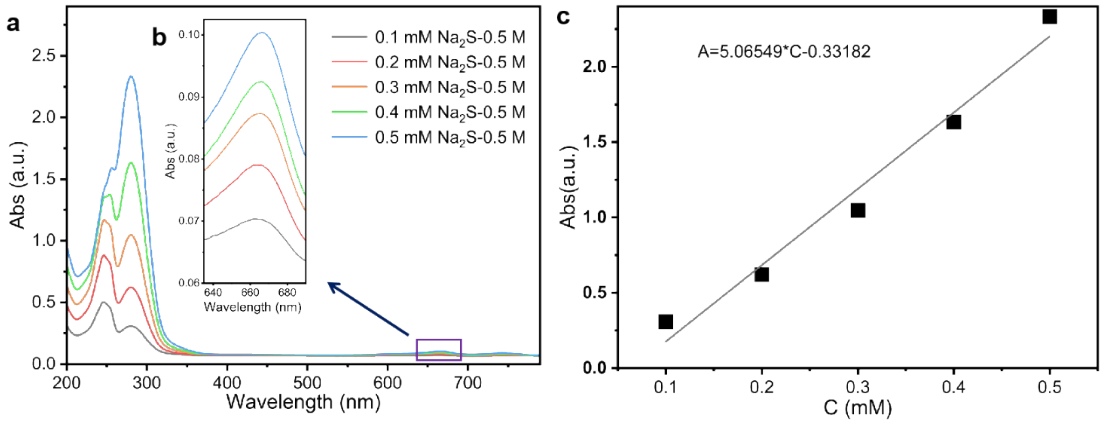

Figure S6. (a, b) UV-vis spectra of external calibration standard using a Na_2S solution; (c) Calibration curve of Na_2S in UV-vis ($R^2 = 0.999$) at 660 nm.

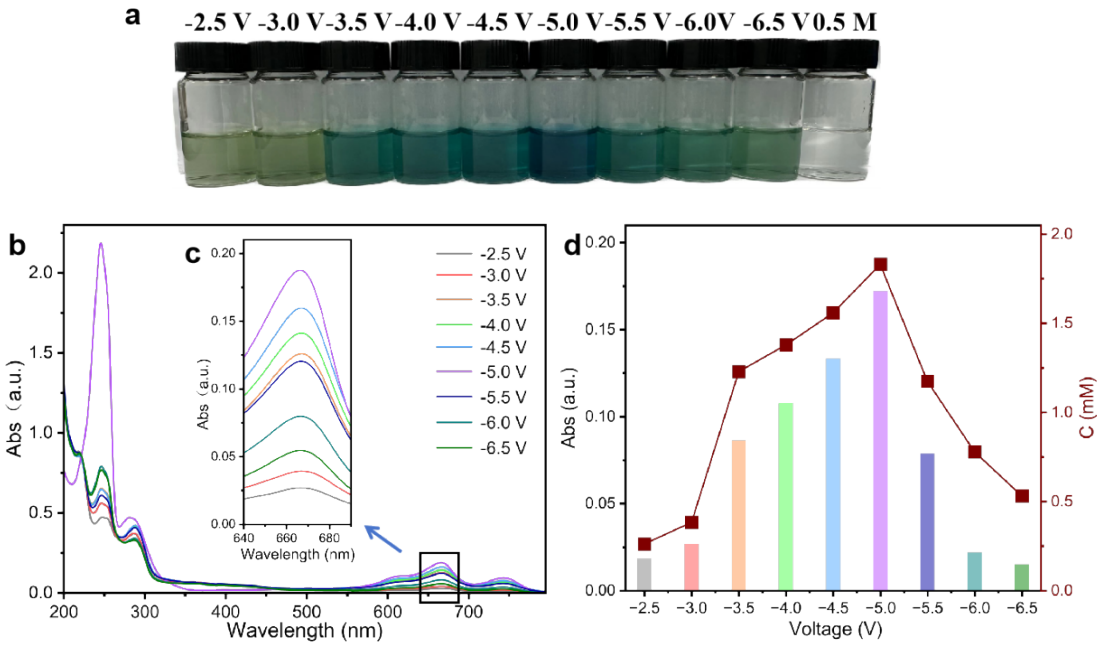

Figure S7. (a) Colorimetry using a commercial sulfide test kit to determine the presence of extracted sulfide after electrochemical desulfurization; (b, c) UV-vis spectra of the extracted S solutions; (d) Concentrations of the extracted sulfur under various voltages.

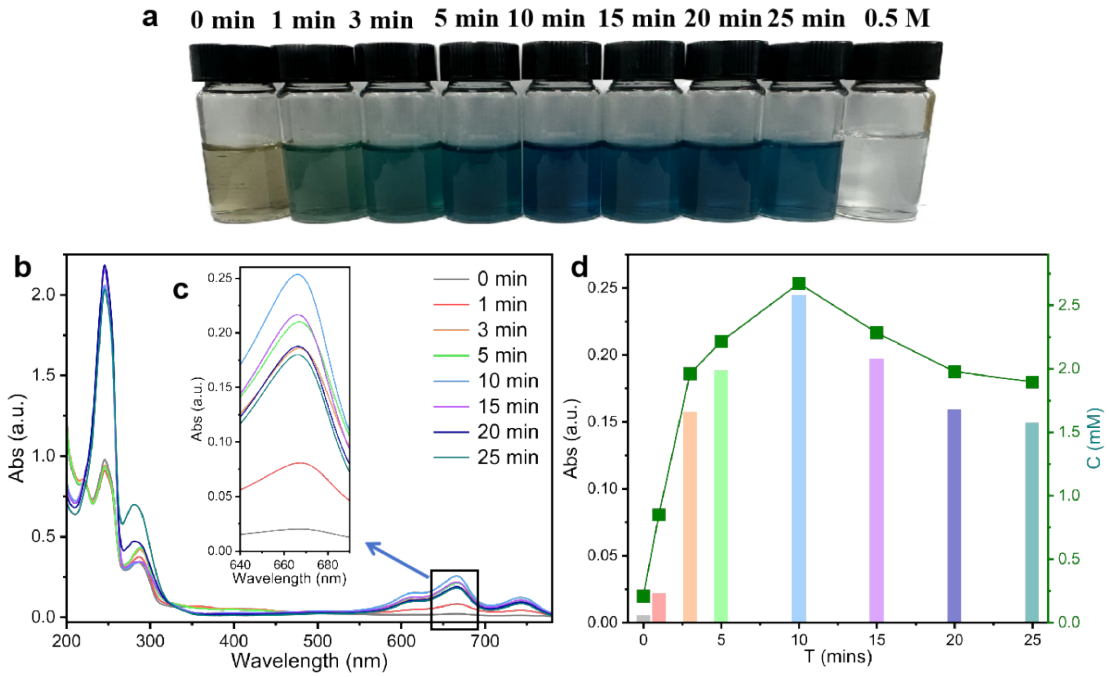

Figure S8. (a) Colorimetry using a commercial sulfide test kit to determine the presence of extracted sulfide after electrochemical desulfurization; (b, c) UV-vis spectra of the extracted S solutions; (d) Concentrations of the extracted sulfur after various periods.

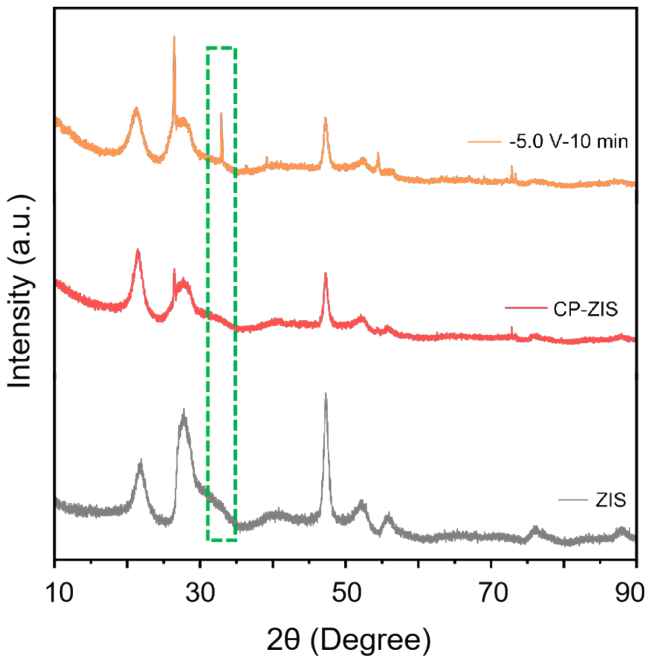

Figure S9. The XRD patterns of ZIS, CP-ZIS, and the sample after sulfur extraction for 10 minutes at -5.0 V, showing the appearance of XRD peaks from carbon paper due to the detachment of ZIS.

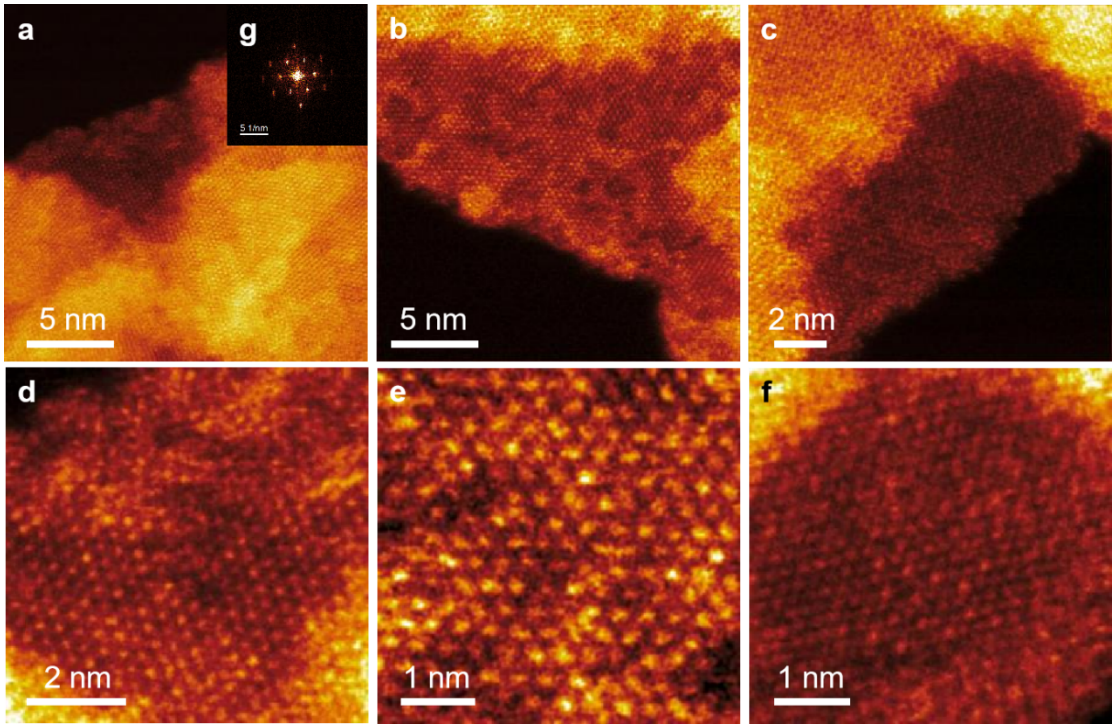

Figure S10. (a-f) Atomic resolution STEM images of monometallic Sv-ZIS-Co; (g) selected area electron diffraction (SAED) pattern of (a), showing a highly crystalline structure of ZIS.

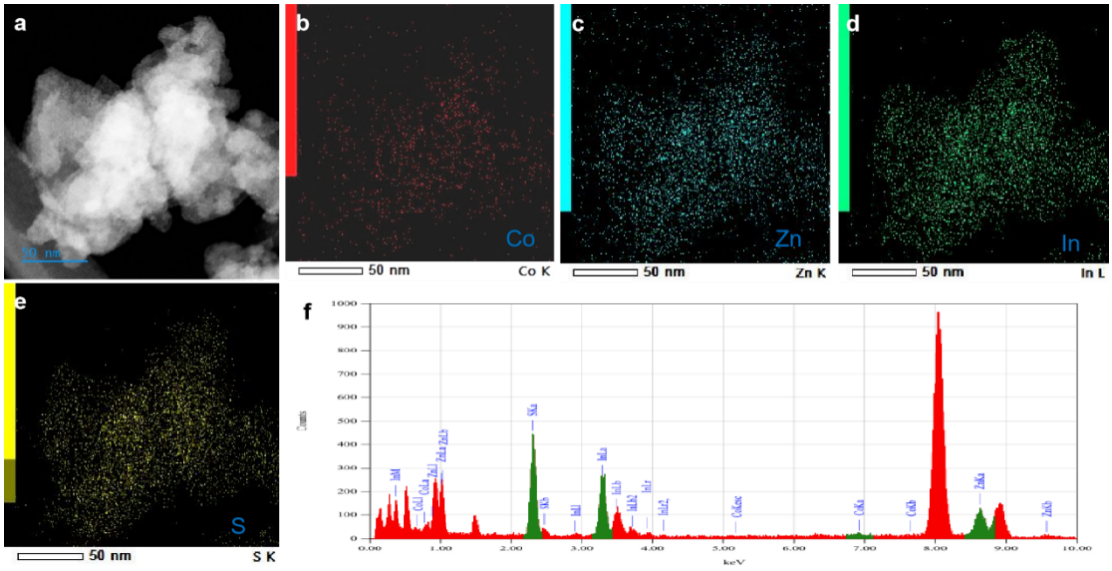

Figure S11. (a-e) The EDS mappings and (f) corresponding energy spectrum of monometallic Sv-ZIS-Co, showing the uniform distribution of Co across the sample.

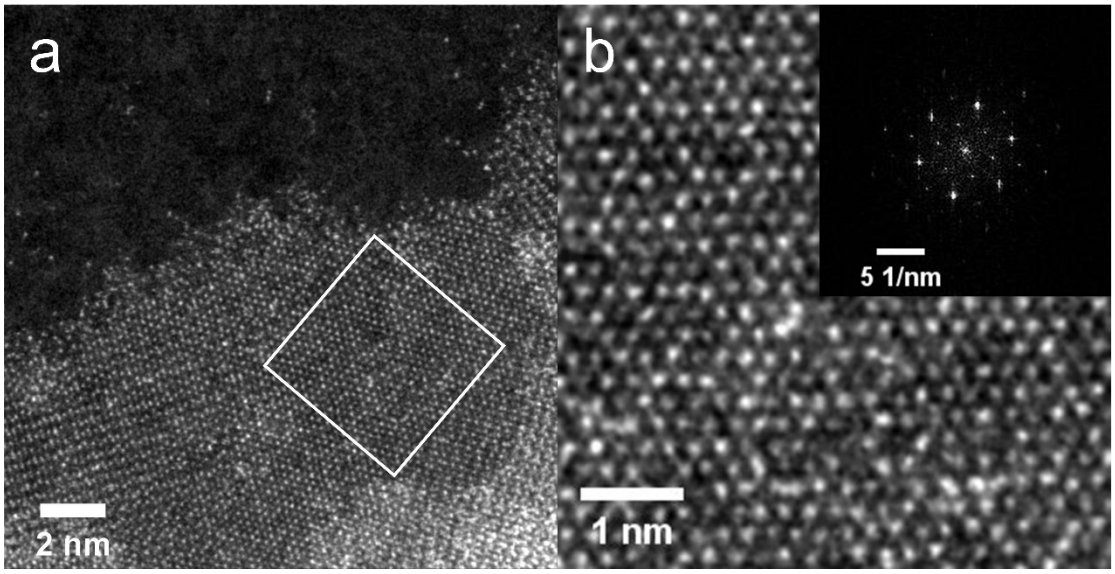

Figure S12. HAADF-STEM images of Sv-ZIS-CoNi without false color. (a) Atomic resolution HAADF-STEM image and (b) the enlarged view of the white box in (a). The inset shows the corresponding SAED pattern;

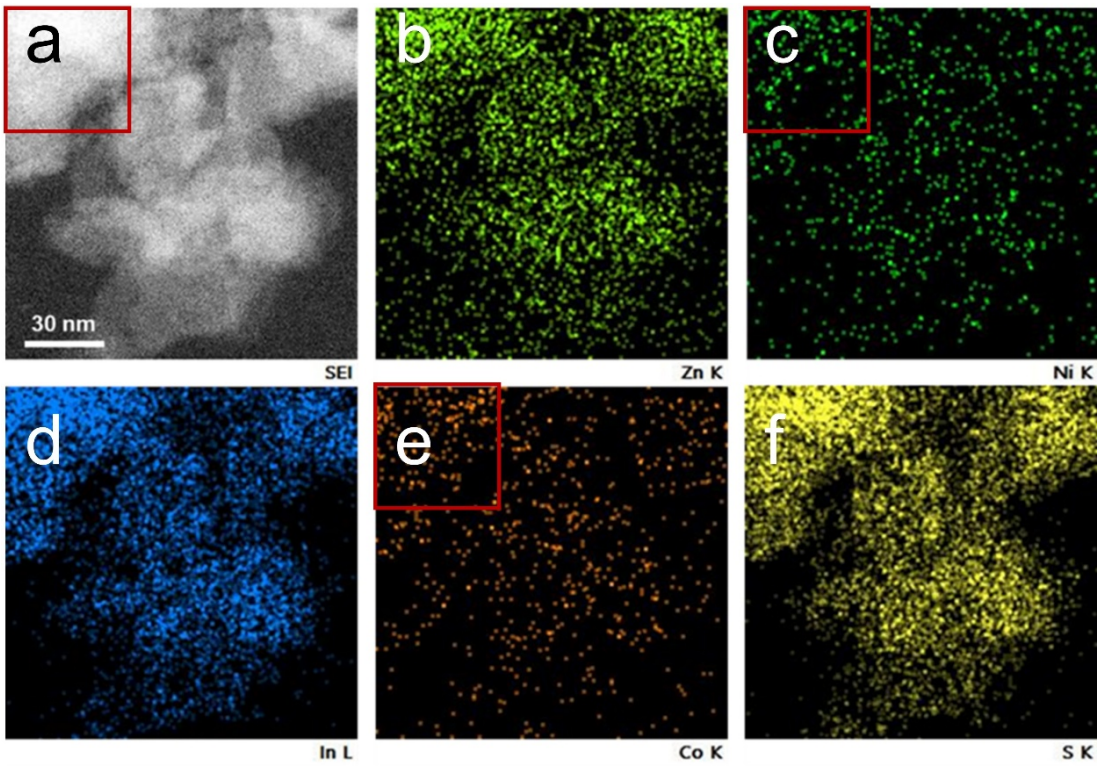

Figure S13. (a-f) Filtered EDS mappings of Sv-ZIS-CoNi.

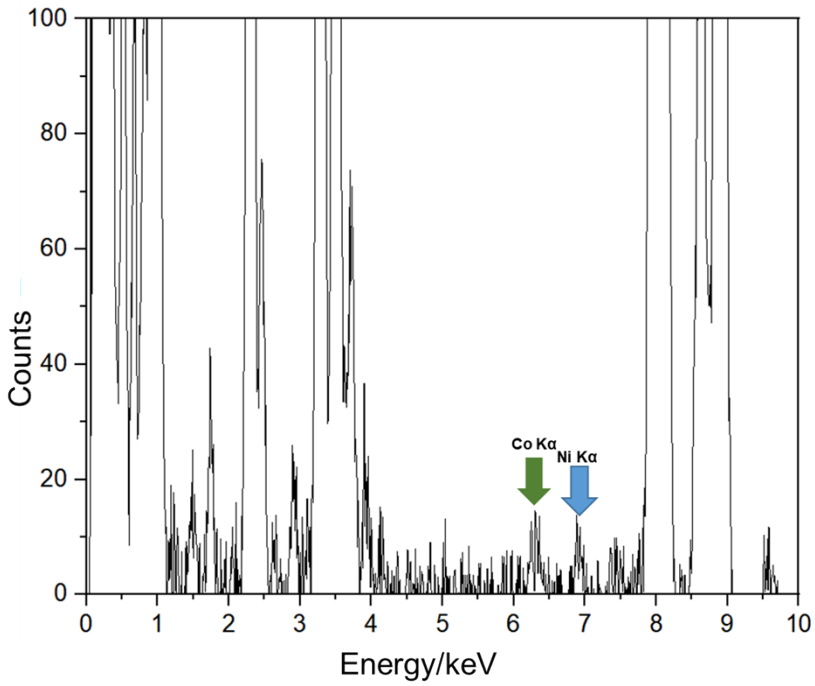

Figure S14. Background-subtracted EDS elemental spectrum of Sv-ZIS-CoNi.

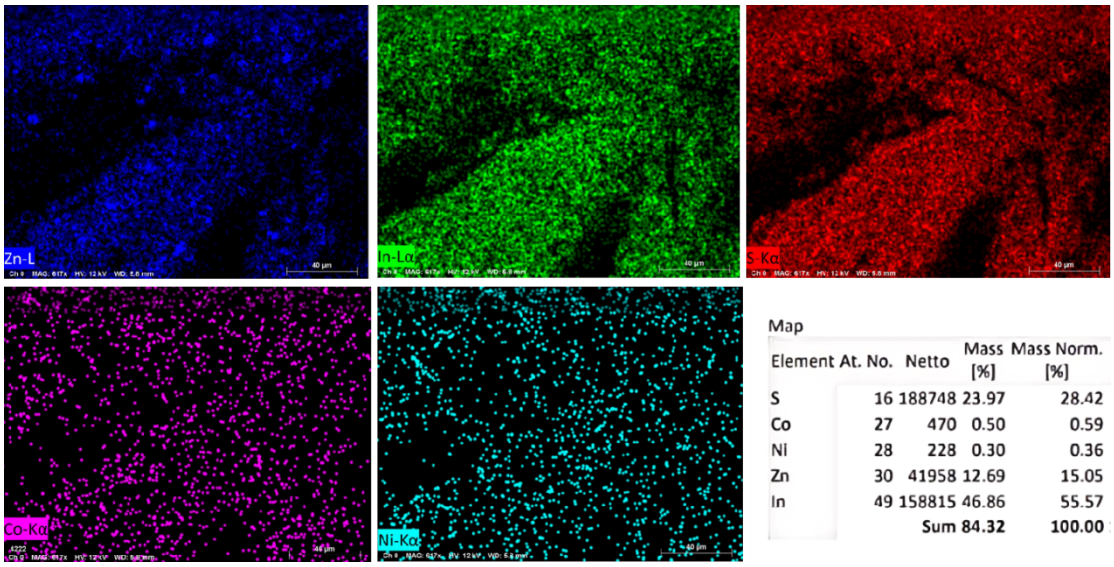

Figure S15. The EDS mappings of the sample without electrochemical desulfurization.

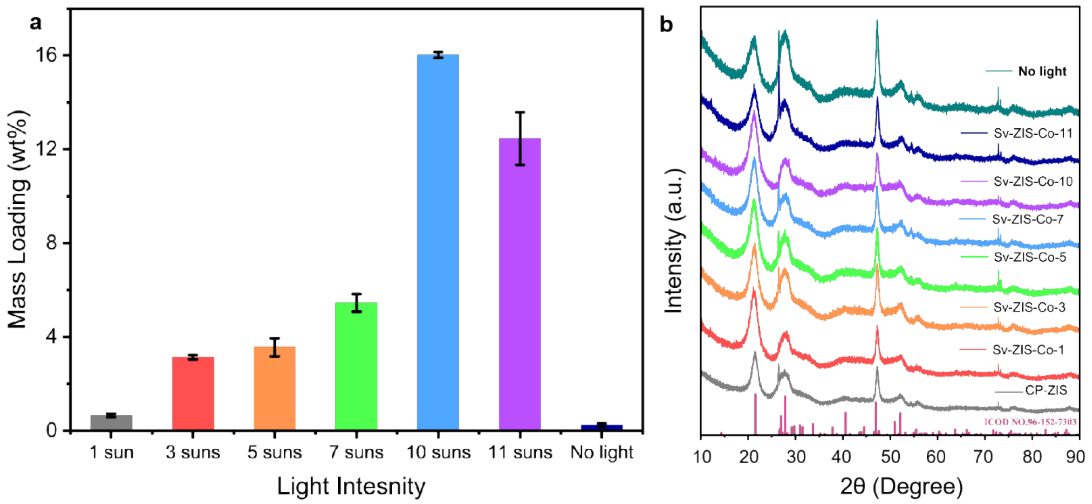

Figure S16. (a) The mass loading of Co single atoms in monometallic Sv-ZIS-Co under various light intensities and (b) the corresponding XRD patterns.

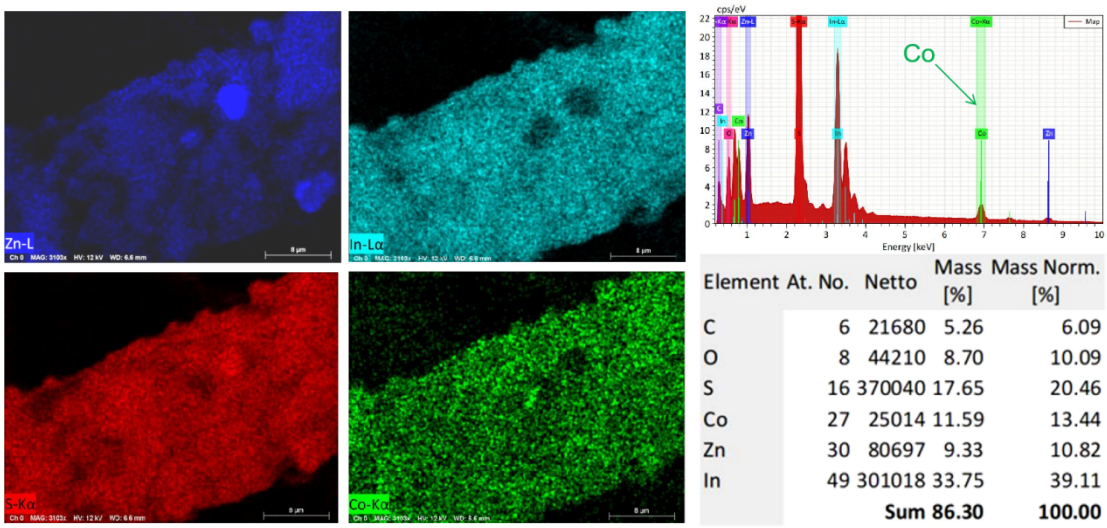

Element	At. No.	Netto	Mass [%]	Mass Norm. [%]
C	6	21680	5.26	6.09
O	8	44210	8.70	10.09
S	16	370040	17.65	20.46
Co	27	25014	11.59	13.44
Zn	30	80697	9.33	10.82
In	49	301018	33.75	39.11
			Sum 86.30	**100.00**

Figure S17. The EDS mappings and the corresponding energy spectrum of Sv-ZIS-Co under a light intensity of 10 suns. The loading of Co is determined as 16.1 wt%.

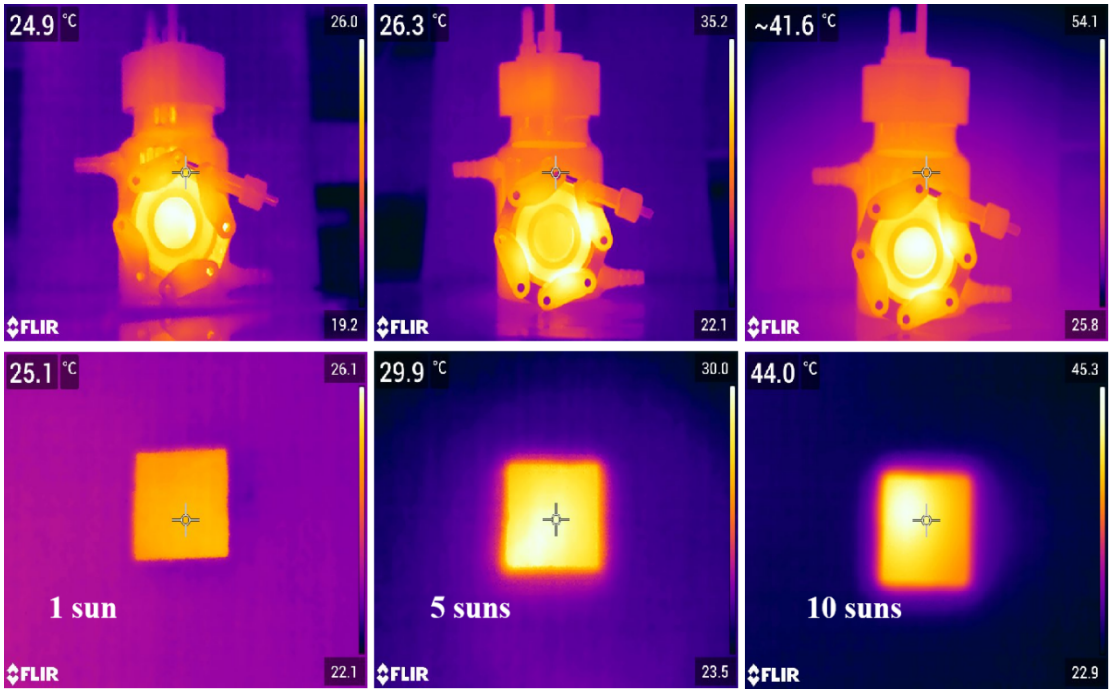

Figure S18. Validation of photothermal effect during photodeposition of single atoms, showing the surface temperatures of the CP-ZISs under various light intensities (suns).

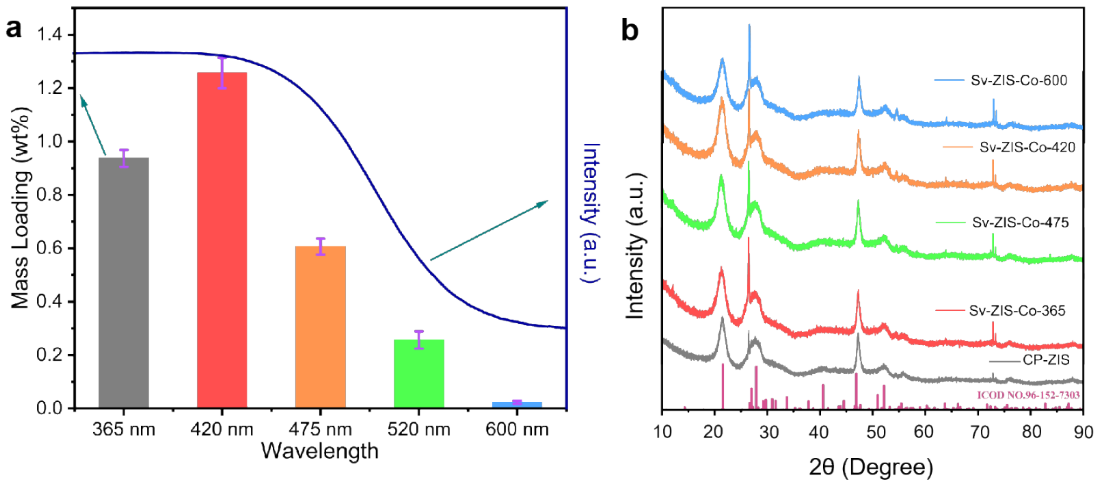

Figure S19. (a) Wavelength dependence of photodeposition in preparing monometallic Sv-ZIS-Co, showing a good correlation between the mass loading of Co (left) and the UV absorption spectrum of ZIS (right); (b) the corresponding XRD patterns.

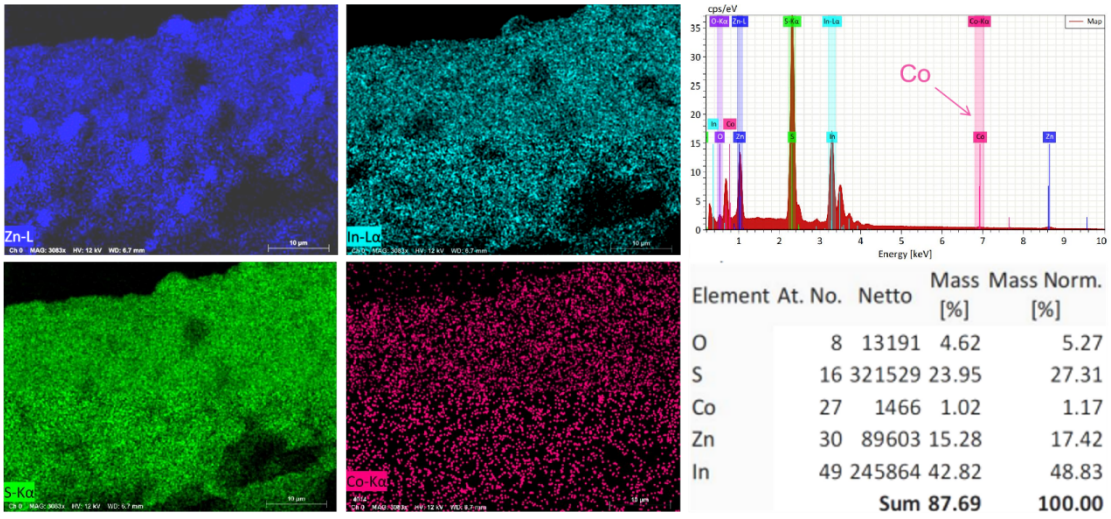

Element	At. No.	Netto	Mass [%]	Mass Norm. [%]
O	8	13191	4.62	5.27
S	16	321529	23.95	27.31
Co	27	1466	1.02	1.17
Zn	30	89603	15.28	17.42
In	49	245864	42.82	48.83
			Sum	**87.69**	**100.00**

Figure S20. The EDS mappings and the corresponding energy spectrum of the Sv-ZIS-Co under a light intensity of 10 suns with a 420 nm cut-off wavelength. The loading of Co is determined as 1.2 wt%.

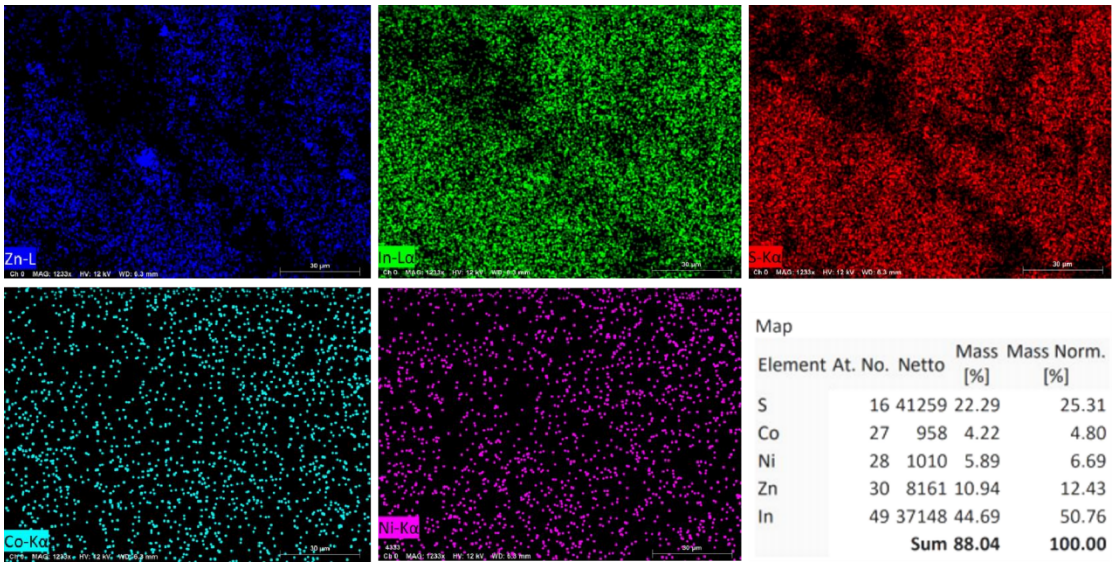

Figure S21. The EDS mappings of bimetallic Sv-ZIS-CoNi. The Co and Ni loadings are determined to be 4.8 and 6.7 wt%, respectively.

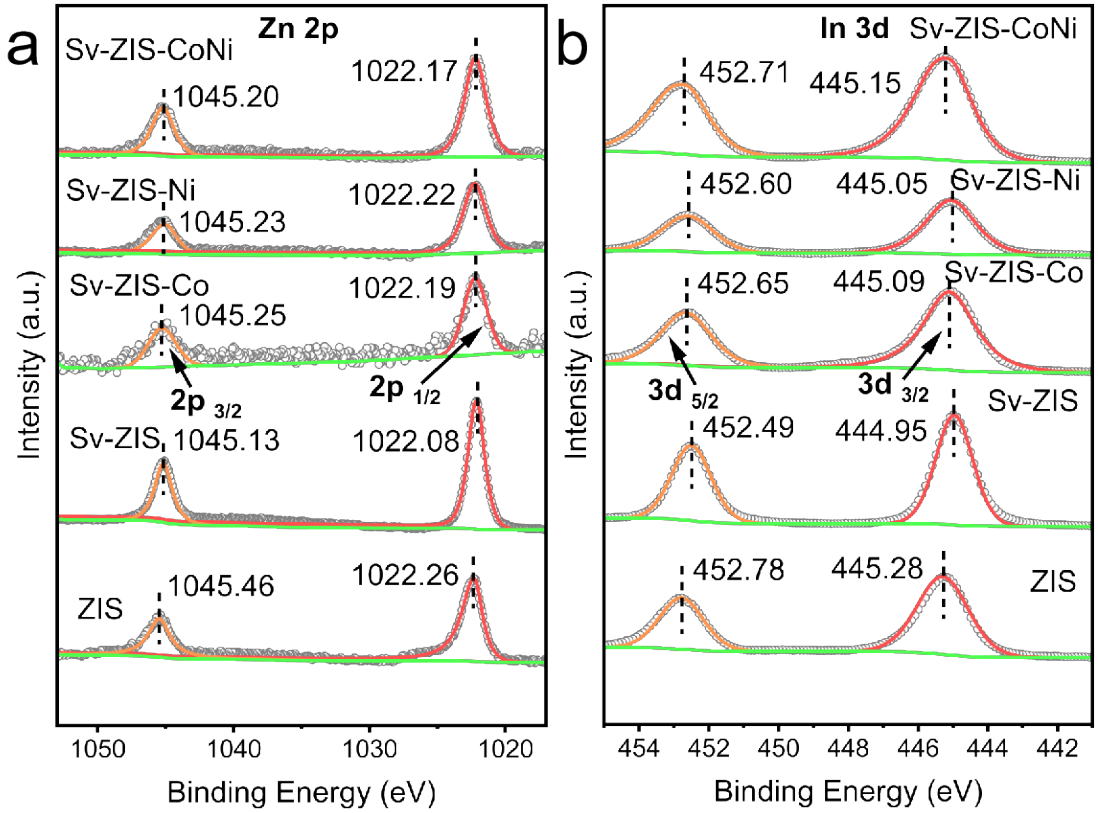

Figure S22. (a) XPS Zn 2p and (b) In 3d core-level spectra of ZIS, Sv-ZIS, monometallic Sv-ZIS-Co, Sv-ZIS-Ni, and bimetallic Sv-ZIS-CoNi.

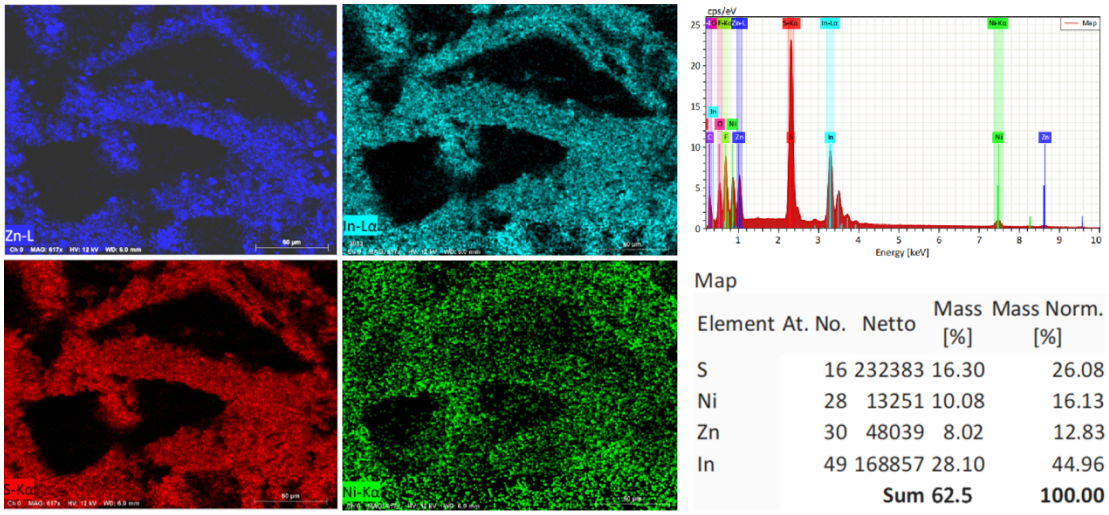

Element	At. No.	Netto	Mass [%]	Mass Norm. [%]
S	16	232383	16.30	26.08
Ni	28	13251	10.08	16.13
Zn	30	48039	8.02	12.83
In	49	168857	28.10	44.96
		Sum	**62.5**	**100.00**

Figure S23. The EDS mappings and the corresponding energy spectrum of Sv-ZIS-Ni. The Ni loading is determined as 16.1 wt%.

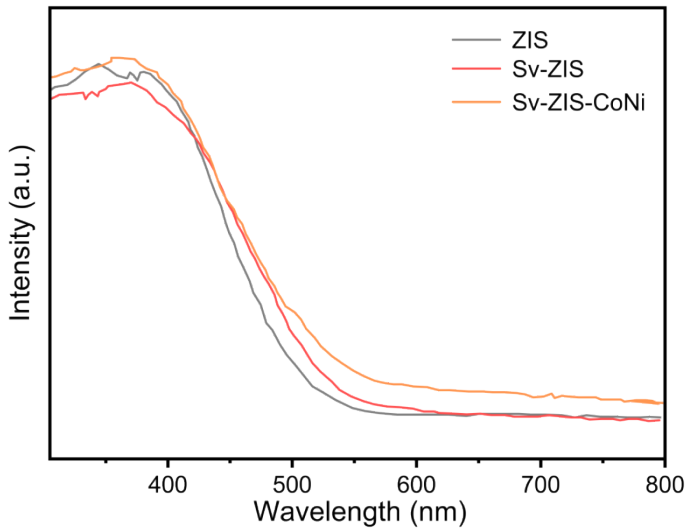

Figure S24. The UV absorption spectra of pristine ZIS, defective ZIS (Sv-ZIS), and bimetallic Sv-ZIS-CoNi.

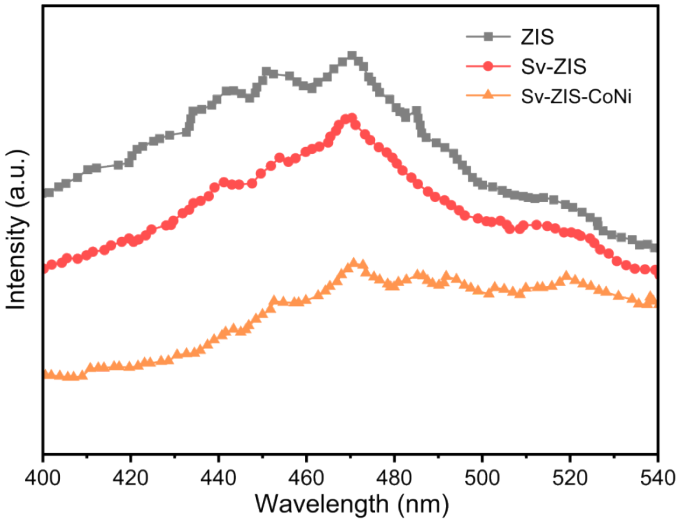

Figure S25. The photoluminescence (PL) spectra of pristine ZIS, defective ZIS (Sv-ZIS), and bimetallic Sv-ZIS-CoNi.

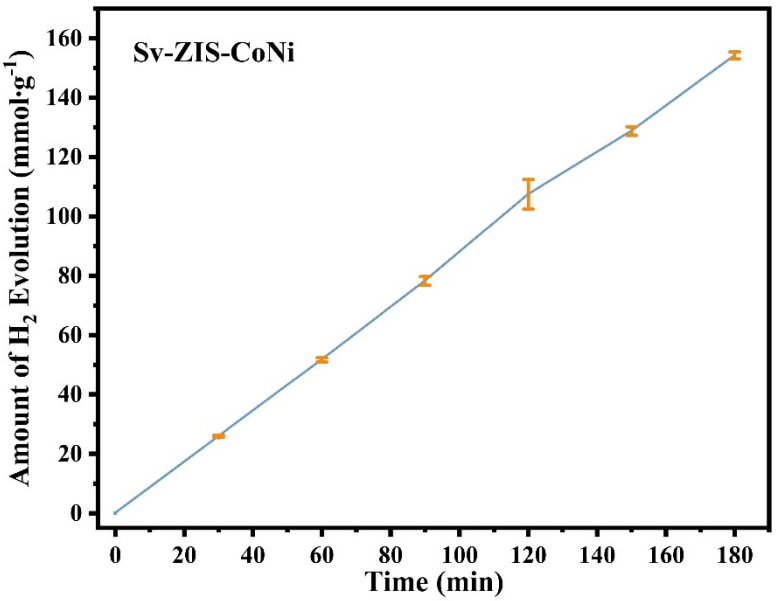

Figure S26. Time-dependent hydrogen evolution over Sv-ZIS-CoNi. Data points represent the mean values from repeated measurements, and the error bars indicate the standard error, highlighting the reproducibility and experimental variability.

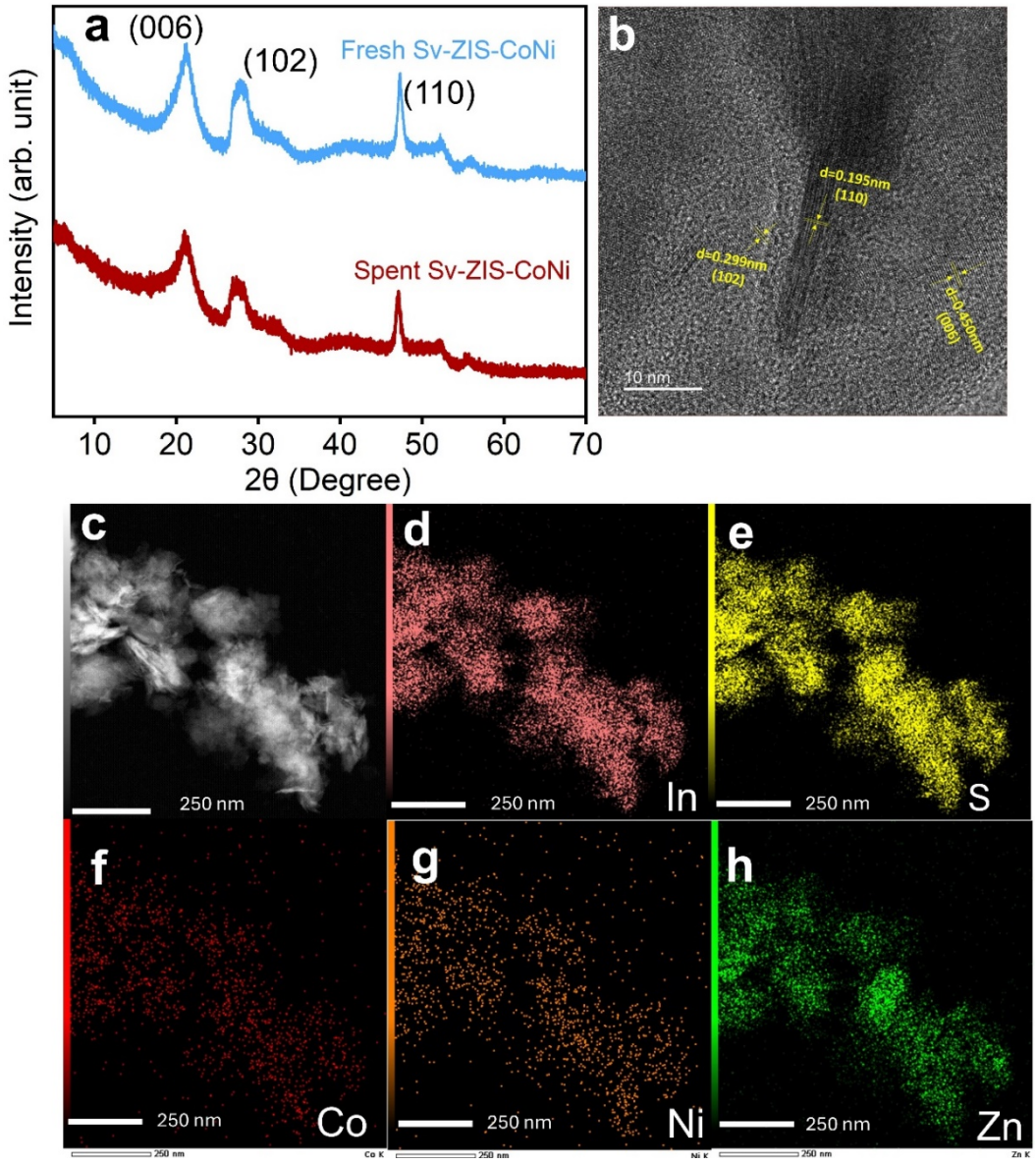

Figure S27. Post-reaction structural and compositional characterization of Sv-ZIS-CoNi. (a) XRD patterns of fresh and spent Sv-ZIS-CoNi, showing that the characteristic reflections can still be identified after reaction, indicative of the retained crystalline structure; (b) HRTEM image of the spent sample, revealing clear lattice fringes with interplanar spacings of 0.450 nm (006), 0.299 nm (102), and 0.195 nm (110); (c) Dark field STEM image and corresponding EDS elemental mappings of (d) In, (e) S, (f) Co, (g) Ni, and (h) Zn for the spent Sv-ZIS-CoNi, confirming the homogeneous spatial distribution of all constituent elements after catalysis.

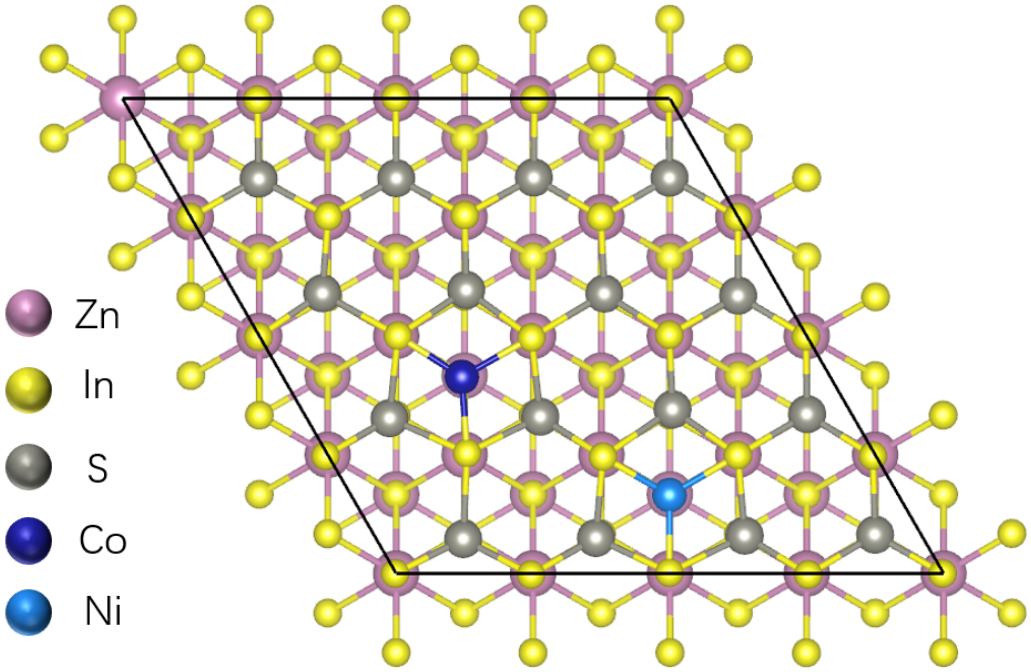

Figure S28. The optimized adsorption configuration of Co/Ni single atoms on the ZIS surface. Color scheme: pink for Zn, yellow for In, grey for S, dark blue for Co, and light blue for Ni.

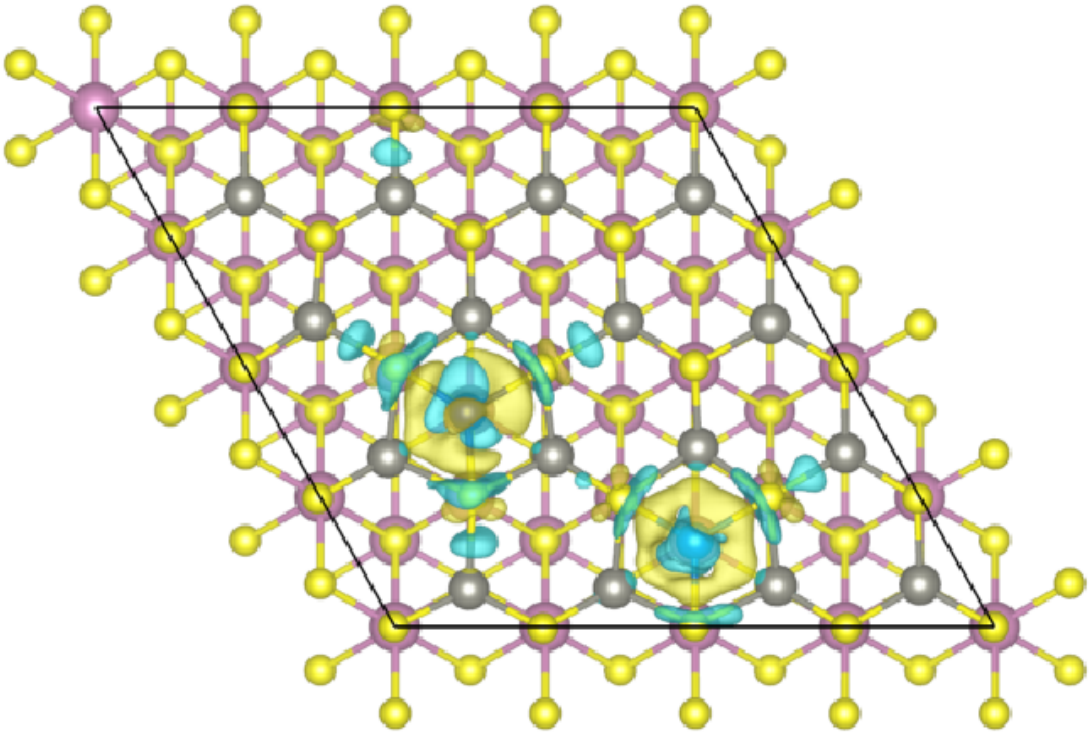

Figure S29. The differential charge density of Sv-ZIS-CoNi, showing the electron accumulation (yellow) and depletion (cyan) regions. The color scheme used is as follows: purple for Zn, yellow for In, grey for S, dark blue for Co, and light blue for Ni.

Table S1. The amount of sulfur extraction at different voltages for 5 minutes.

Voltage (V)	Concentration (mM)	H_2S (mg)	Degree of sulfur extraction (%)
-2.5	0.179	0.168	0.6
-3.0	0.262	0.247	0.8
-3.5	**0.843**	**0.794**	**2.8**
-4.0	1.052	0.990	3.5
-4.5	1.302	1.226	4.4
-5.0	**1.682**	**1.583**	**5.6**
-5.5	0.767	0.722	2.6
-6.0	0.215	0.202	0.7
-6.5	0.147	0.138	0.5

The operation at more negative voltages (such as -5.0 V) results in structural distortion of ZIS in the XRD patterns and the emergence of unwanted $Zn_3In_2S_6$ phases. To this end, an optimal voltage of -2.5 V, without structural distortion, was selected for further studies, which yielded a desulfurization degree of 0.6%.

Table S2. The amount of sulfur extraction after various periods at -3.5 V.

Time (minutes)	Concentration (mM)	H_2S (mg)	Degree of sulfur extraction (%)
0	0.056	0.058	0.2
1	0.228	0.234	0.7
3	1.659	1.695	5.7
5	1.988	2.031	6.8
10	**2.579**	**2.635**	**8.9**
15	2.077	2.122	7.1
20	1.682	1.718	5.8
25	1.576	1.611	5.4

Table S3. Effect of concentration and deposition sequence on photodeposition.

Sample	Co (wt%)	Ni (wt%)
Sv-ZIS-10 Co-10 Ni	0.4	10.6
Sv-ZIS-10 Co-1 Ni	1.7	5.3
Sv-ZIS-10 Ni-10 Co	1.1	1.5
Sv-ZIS-10 Co & 10 Ni	1.0	7.5
Sv-ZIS-10Co & 1 Ni	3.0	4.0

Samples were prepared under 10 suns for 1.5 hours. Sv-ZIS-10 Co-10 Ni was prepared by sequential deposition of Co in 10 mM $CoCl_2$ and then Ni in 10 mM $NiCl_2$. Sv-ZIS-10 Co & 10 Ni was prepared by co-deposition of Co and Ni in 10 mM $CoCl_2$ and 10 mM $NiCl_2$ simultaneously. We found that the deposition sequence and concentration of metal precursor have a profound impact on the final metal loading of bimetallic Sv-ZIS-CoNi samples.

Table S4. Effect of light intensity on photodeposition for 1.5 hours.

Light intensity	Co (wt%)	Ni (wt%)
10 suns	3.5	4.7
15 suns	3.9	11.9

Samples were prepared by co-deposition in 10 mM of $CoCl_2$ and 10 mM of $NiCl_2$.

Table S5. Effect of irradiation period on photodeposition.

Period (hour)	Co (wt%)	Ni (wt%)
1.5	3.5	4.7
2.5	5.0	7.0
3.0	3.9	11.1

Samples were prepared by co-deposition in 10 mM of $CoCl_2$ and 10 mM of $NiCl_2$.

Table S6. Effect of concentration in an optimal deposition period (1.5 hours) and light intensity (10 suns).

Concentration (mM)	Co (wt%)	Ni (wt%)
10 mM $CoCl_2$ & 10 mM $NiCl_2$	3.5	4.7
20 mM $CoCl_2$ & 20 mM $NiCl_2$	4.6	6.9

Table S7. Effect of catalyst loading (on CP) on photodeposition.

15 mg cm^{-2}	Co (wt%)	Ni (wt%)	8 mg cm^{-2}	Co (wt%)	Ni (wt%)
1.5 hours	3.5	4.7	1.5 hours	3.7	4.8
2.5 hours	5.0	7.0	2.5 hours	4.1	5.8
3.0 hours	3.9	11.1	3.0 hours	4.0	5.2

Table S8. The optimal samples of monometallic and bimetallic SACs.

Sample	Co (wt%)	Ni (wt%)
Sv-ZIS-Co	14 ~ 16%	--
Sv-ZIS-Ni	--	14 ~ 16%
Sv-ZIS-CoNi	~ 5%	~ 6%
ZIS-CoNi *	N.D.	N.D.

* ZIS-CoNi stands for the sample prepared without electrochemical desulfurization. Co and Ni single-atoms were unable to deposit on unmodified ZIS via photodeposition.

Table S9. The elementary composition results from XPS

Element	Area	Atom (%)	Element	Area	Atom%
C 1s	21038	34.98	S 2p	27748	22.75
Zn 2p	65433	6.86	Co 2p	44300	7.61
In 3d	326904	18.81	Ni 2p	81343	10.29

Table S10. Performance tracker for the photocatalytic hydrogen (H_2) evolution over $ZnIn_2S_4$-based photocatalysts.

Photocatalyst	Sacrificial agent	Light source	H_2 evolution rate (mmol g^{-1} h^{-1})	Ref.
Co-P/$ZnIn_2S_4$	10 vol.% lactic acid	300 W Xe lamp (λ > 420 nm)	7.84	(11)
Co-doped $ZnIn_2S_4$	0.25 M Na_2SO_3 + 0.35 M Na_2S	500 W Xe lamp (λ> 400 nm)	1.00	(12)
O-doped $ZnIn_2S_4$	0.25 M Na_2SO_3 + 0.35 M Na_2S	300 W Xe lamp (λ > 420 nm)	2.12	(13)
N-doped $ZnIn_2S_4$	10 vol.% TEOA	300 W Xe lamp (λ > 400 nm)	11.09	(14)
$ZnIn_2S_4$ with sulfur vacancies	10 vol.% TEOA	300 W Xe lamp (λ > 400 nm)	13.48	(15)
$ZnIn_2S_4$ with active (110) facet exposure	20 vol.% TEOA	300 W Xe lamp (λ > 420 nm)	1.94	(16)
MWCNTs/$ZnIn_2S_4$	0.25 M Na_2SO_3 + 0.35 M Na_2S	300 W Xe lamp (λ > 420 nm)	6.84	(17)
Carbon nanofiber @$ZnIn_2S_4$	0.25 M Na_2SO_3 + 0.35 M Na_2S	300 W Xe lamp (λ > 420 nm)	3.17	(18)
Carbon nanodots /$ZnIn_2S_4$	0.25 M Na_2SO_3 + 0.35 M Na_2S	300 W Xe lamp (λ > 420 nm)	4.15	(19)
Co/NGC@$ZnIn_2S_4$	1 mL TEOA + 5 mL H_2O	300 W Xe lamp (λ > 400 nm)	11.27	(20)
$ZnIn_2S_4$ with sulfur vacancies/*g*-C_3N_4	20 vol.% TEOA	300 W Xe lamp (λ > 420 nm)	6.10	(21)
Mo_2C/$ZnIn_2S_4$	10 vol.% TEOA	300 W Xe lamp (λ > 400 nm)	22.11	(22)
$ZnIn_2S_4$/CdS	0.25 M Na_2SO_3 + 0.35 M Na_2S	300 W Xe lamp (λ > 400 nm)	5.68	(23)

$L_{40}N_5ZIS$	0.25 M Na_2SO_3 + 0.35 M Na_2S	300 W Xe lamp (λ > 420 nm)	9.74	(24)
Co_9S_8@$ZnIn_2S_4$	20 vol.% TEOA	300 W Xe lamp (λ > 400 nm)	6.25	(25)
$ZnIn_2S_4/CdIn_2S_4$	0.25 M Na_2SO_3 + 0.35 M Na_2S	300 W Xe lamp (λ > 420 nm)	12.67	(26)
$ZnIn_2S_4/NaNbO_3$	10 vol.% TEOA	300 W Xe lamp	30.04	(27)
$ZnIn_2S_4/CaTiO_3$	0.25 M Na_2SO_3 + 0.35 M Na_2S	300 W Xe lamp (λ > 420 nm)	22.19	(28)
$ZnIn_2S_4/Mo_2C$	10 vol.% TEOA	300 W Xe lamp AM 1.5 G	42.80	(29)
g-$C_3N_4/ZnIn_2S_4$/NiS	10 vol.% lactic acid	300 W Xe lamp (λ > 420 nm)	16.31	(30)
$CuInS_2/ZnIn_2S_4$	0.25 M Na_2SO_3 + 0.35 M Na_2S	150 W Xe lamp (λ > 420 nm)	3.43	(31)
Sv-ZIS-CoNi	**10 vol.% TEOA**	**300 W Xe lamp (λ > 420 nm)**	**51.47**	**This work**

Table S11. The turnover frequency (TOF) value of SACs in catalytic performance.

Catalyst	H_2 evolution rate (mmol g^{-1} h^{-1})	Method	Co loading	Ni loading	TOF (h^{-1})
Sv-ZIS-Co	33.0	EDS	16.1 wt%	N.A.	12.1
Sv-ZIS-Ni	35.2	EDS	N.A.	16.1 wt%	12.8
Sv-ZIS-CoNi	**51.5**	**EDS**	**4.8 wt%**	**6.7 wt%**	**27.8**
		XPS	**7.6 atom%**	**10.3 atom%**	**23.0**

The influence of vacancy is not considered in the TOF calculation.

Table S12. Details on the light intensity and catalytic performance at various wavelengths, and the results of AQY.

Wavelength (nm)	The mean H_2 production in 30 mins	Light power (Xe lamp)
375	15.8 μmol	0.070 W
420	35.6 μmol	0.170 W
475	31.5 μmol	0.247 W
520	17.8 μmol	0.354 W
600	0.57 μmol	0.223 W

Detailed calculations of the AQYs at various wavelengths:

(1) λ = 375 nm,

$$N = \frac{\mathrm{Pt}\lambda}{\mathrm{hc}} = \frac{0.070 \times 1800 \times 375 \times 10^{-9}}{6.626 \times 10^{-34} \times 3 \times 10^{8}} = 2.4 \times 10^{20}$$

$$AQY = \frac{4 \times 15.8 \times 10^{-6} \times 6.02 \times 10^{23}}{2.4 \times 10^{20}} \times 100\% = 15.9\%$$

(2) λ = 420 nm,

$$N = \frac{\mathrm{Pt}\lambda}{\mathrm{hc}} = \frac{0.170 \times 1800 \times 420 \times 10^{-9}}{6.626 \times 10^{-34} \times 3 \times 10^{8}} = 6.5 \times 10^{20}$$

$$AQY = \frac{4 \times 35.6 \times 10^{-6} \times 6.02 \times 10^{23}}{6.5 \times 10^{20}} \times 100\% = 13.2\%$$

(3) λ = 475 nm,

$$N = \frac{\mathrm{Pt}\lambda}{\mathrm{hc}} = \frac{0.247 \times 1800 \times 475 \times 10^{-9}}{6.626 \times 10^{-34} \times 3 \times 10^{8}} = 1.1 \times 10^{21}$$

$$AQY = \frac{4 \times 31.5 \times 10^{-6} \times 6.02 \times 10^{23}}{1.1 \times 10^{21}} \times 100\% = 6.9\%$$

(4) λ = 520 nm,

$$N = \frac{\mathrm{Pt}\lambda}{\mathrm{hc}} = \frac{0.354 \times 1800 \times 520 \times 10^{-9}}{6.626 \times 10^{-34} \times 3 \times 10^{8}} = 1.7 \times 10^{21}$$

$$AQY = \frac{4 \times 17.8 \times 10^{-6} \times 6.02 \times 10^{23}}{1.7 \times 10^{21}} \times 100\% = 2.5\%$$

(5) λ = 600 nm,

$$N = \frac{\mathrm{Pt}\lambda}{\mathrm{hc}} = \frac{0.223 \times 1800 \times 600 \times 10^{-9}}{6.626 \times 10^{-34} \times 3 \times 10^{8}} = 1.2 \times 10^{21}$$

$$AQY = \frac{4 \times 0.57 \times 10^{-6} \times 6.02 \times 10^{23}}{1.2 \times 10^{21}} \times 100\% = 0.1\%$$

REFERENCE

1. Baerends, E. Perspective on "Self-consistent equations including exchange and correlation effects". Theor. Chem. Acc. **2000**, 103. DOI: 10.1007/s002140050031.

2. Bobrov, V.; Trigger, S. To the Theory of Inhomogeneous Electron Gas. Tech Phys. **2018**, 63. DOI: 10.1134/S1063784218080030.

3. BLOCHL, P. Projector augmented-wave method. Phys Rev B. **1994**, 50. DOI: 10.1103/PhysRevB.50.17953.

4. Kresse, G.; Furthmuller, J. Efficient iterative schemes for ab initio total-energy calculations using a plane-wave basis set Phys Rev B. **1996**, 54. DOI: 10.1103/PhysRevB.54.11169.

5. Perdew, J.; Burke, K.; Ernzerhof, M. Generalized Gradient Approximation Made Simple. Phys. Rev. Lett. **1996**, 77. DOI: 10.1103/PhysRevLett.78.1396.

6. Grimme, S.; Antony, J.; Ehrlich, S.; Krieg, H. A consistent and accurate ab initio parametrization of density functional dispersion correction (DFT-D) for the 94 elements H-Pu. J. Chem. Phys. **2010**, 132, 154104. DOI: 10.1063/1.3382344.

7. Li, G.; Liang, H.; Fan, X.; Lv, X.; Sun, X.; Wang, H.; Bai, J. Modulating and optimizing 2D/2D Fe-Ni_2P/$ZnIn_2S_4$ with S vacancy through surface engineering for efficient photocatalytic H_2 evolution. J Mater Chem A. **2023**, 11. DOI: 10.1039/d3ta02519e.

8. Li, Z.; Wang, X.; Tian, W.; Meng, A.; Yang, L. CoNi Bimetal Cocatalyst Modifying a Hierarchical $ZnIn_2S_4$ Nanosheet-Based Microsphere Noble-Metal-Free Photocatalyst

for Efficient Visible-Light-Driven Photocatalytic Hydrogen Production. ACS Sustainable Chem Eng. **2019**, 7, 20190-20201. DOI: 10.1021/acssuschemeng.9b06430.

9. Wang, X.; Wang, X.; Huang, J.; Li, S.; Meng, A.; Li, Z. Interfacial chemical bond and internal electric field modulated Z-scheme Sv- $ZnIn_2S_4/MoSe_2$ photocatalyst for efficient hydrogen evolution. Nat Commun. **2021**, 12. DOI: 10.1038/s41467-021-24511-z.

10. Chen, W.; Liu, T.; Huang, T.; Liu, X.; Yang, X. Novel mesoporous P-doped graphitic carbon nitride nanosheets coupled with $ZnIn_2S_4$ nanosheets as efficient visible light driven heterostructures with remarkably enhanced photo-reduction activity. Nanoscale. **2016**, 8. DOI: 10.1039/c5nr07695a.

11. Liu, Q.; Wang, M.; He, Y.; Wang, X.; Su, W. Photochemical route for synthesizing Co–P alloy decorated $ZnIn_2S_4$ with enhanced photocatalytic H_2 production activity under visible light irradiation. Nanoscale. **2018**, 10. DOI: 10.1039/c8nr05934a.

12. Wen-Hui, Y.; Xiao-Chen, L. I. U.; Li, L. I. Improving Photocatalytic Performance for Hydrogen Generation over Co-Doped $ZnIn_2S_4$ under Visible Light. Acta Physico-Chimica Sinica. **2013**, 29, 151-156. DOI: 10.3866/pku.whxb201210093.

13. Yang, W.; Zhang, L.; Xie, J.; Zhang, X.; Liu, Q.; Yao, T.; Wei, S.; Zhang, Q.; Xie, Y. Enhanced Photoexcited Carrier Separation in Oxygen-Doped $ZnIn_2S_4$ Nanosheets for Hydrogen Evolution. Angew. Chem. Int. Ed. **2016**, 55, 6716-6720. DOI: 10.1002/anie.201602543.

14. Du, C.; Yan, B.; Lin, Z.; Yang, G. Enhanced carrier separation and increased

electron density in 2D heavily N-doped $ZnIn_2S_4$ for photocatalytic hydrogen production. J Mater Chem A. **2020**, 8. DOI: 10.1039/c9ta11318e.

15. Du, C.; Zhang, Q.; Lin, Z.; Yan, B.; Xia, C.; Yang, G. Half-unit-cell $ZnIn_2S_4$ monolayer with sulfur vacancies for photocatalytic hydrogen evolution. Appl Catal B-Environ. **2019**, 248, 193-201. DOI: 10.1016/j.apcatb.2019.02.027.

16. Shi, X.; Mao, L.; Yang, P.; Zheng, H.; Fujitsuka, M.; Zhang, J.; Majima, T. Ultrathin $ZnIn_2S_4$ nanosheets with active (110) facet exposure and efficient charge separation for cocatalyst free photocatalytic hydrogen evolution. Appl Catal B-Environ. **2020**, 265, 118616. DOI: 10.1016/j.apcatb.2020.118616.

17. Chai, B.; Peng, T.; Zeng, P.; Zhang, X. Preparation of a MWCNTs/$ZnIn_2S_4$ composite and its enhanced photocatalytic hydrogen production under visible-light irradiation. Dalton Trans. **2012**, 41, 1179-1186. DOI: 10.1039/c1dt11308a.

18. Chen, Y.; Tian, G.; Ren, Z.; Pan, K.; Shi, Y.; Wang, J.; Fu, H. Hierarchical Core–Shell Carbon Nanofiber@$ZnIn_2S_4$ Composites for Enhanced Hydrogen Evolution Performance. ACS Appl. Mater. Interfaces. **2014**, 6, 13841-13849. DOI: 10.1021/am5032083.

19. Lei, K.; Kou, M.; Ma, Z.; Deng, Y.; Ye, L.; Kong, Y. A comparative study on photocatalytic hydrogen evolution activity of synthesis methods of CDs/$ZnIn_2S_4$ photocatalysts. Colloids Surf. A Physicochem. Eng. Asp. **2019**, 574, 105-114. DOI: 10.1016/j.colsurfa.2019.04.073.

20. Wang, S.; Wang, Y.; Zhang, S. L.; Zang, S. Q.; Lou, X. W. Supporting Ultrathin

$ZnIn_2S_4$ Nanosheets on Co/N-Doped Graphitic Carbon Nanocages for Efficient Photocatalytic H_2 Generation. Adv. Mater. **2019**, 31. DOI: 10.1002/adma.201903404.

21. Qin, Y.; Li, H.; Lu, J.; Feng, Y.; Meng, F.; Ma, C.; Yan, Y.; Meng, M. Synergy between van der waals heterojunction and vacancy in $ZnIn_2S_4$/g-C_3N_4 2D/2D photocatalysts for enhanced photocatalytic hydrogen evolution. Appl Catal B-Environ. **2020**, 277, 119254. DOI: 10.1016/j.apcatb.2020.119254.

22. Du, C.; Yan, B.; Yang, G. Self-integrated effects of 2D $ZnIn_2S_4$ and amorphous Mo_2C nanoparticles composite for promoting solar hydrogen generation. Nano Energy. **2020**, 76, 105031. DOI: 10.1016/j.nanoen.2020.105031.

23. Li, C. Q.; Du, X.; Jiang, S.; Liu, Y.; Niu, Z. L.; Liu, Z. Y.; Yi, S. S.; Yue, X. Z. Constructing Direct Z-Scheme Heterostructure by Enwrapping $ZnIn_2S_4$ on CdS Hollow Cube for Efficient Photocatalytic H_2 Generation. Adv Sci. **2022**, 9, e2201773. DOI: 10.1002/advs.202201773.

24. Geng, Z.; Bo, T.; Zhou, W.; Tan, X.; Ye, J.; Yu, T. Deciphering the Superior Electronic Transmission Induced by the Li-N Ligand Pairs Boosted. small. **2023**. DOI: 10.1002/smll.202206673.

25. Wang, S.; Guan, B. Y.; Wang, X.; Lou, X. W. D. Formation of Hierarchical Co_9S_8@ $ZnIn_2S_4$ Heterostructured Cages as an Efficient Photocatalyst for Hydrogen Evolution. J. Am. Chem. Soc. **2018**, 140, 15145-15148. DOI: 10.1021/jacs.8b07721.

26. Dang, X.; Xie, M.; Dai, F.; Guo, J.; Liu, J.; Lu, X. The in situ construction of $ZnIn_2S_4$/$CdIn_2S_4$ 2D/3D nano hetero-structure for an enhanced visible-light-driven

hydrogen production. J Mater Chem A. **2021**, 9. DOI: 10.1039/d1ta02052h.

27. Zhang, J.; Gu, H.; Wang, X.; Zhang, H.; Li, L.; Wang, X.; Dai, W. Facile and robust construction of a 3D-hierarchical $NaNbO_3$-nanorod/$ZnIn_2S_4$ heterojunction towards ultra-high photocatalytic H_2 production. Catal Sci Technol. **2022**, 12. DOI: 10.1039/d2cy00115b.

28. Dai, F.; Wang, Y.; Zhao, R.; Zhou, X.; Han, J.; Wang, L. $ZnIn_2S_4$ modified $CaTiO_3$ nanocubes with enhanced photocatalytic hydrogen performance. Int. J. Hydrogen Energy. **2020**, 45, 28783-28791. DOI: 10.1016/j.ijhydene.2020.07.228.

29. Ma, C.; Pan, J.; Guan, Y.; Wang, Y.; Wu, S.; Du, Z.; Sun, M.; Gao, Z.; Tang, H.; Yan, X. Step-type charge transfer path enhanced photothermal catalytic hydrogen production performance of 3D/2D Mo_2C/$ZnIn_2S_4$ composites. Ceram. Int. **2025**, 51, 21384-21392. DOI: 10.1016/j.ceramint.2025.02.298.

30. Xia, Y.; He, Y.; Liu, X.; Huang, R.; Liang, R.; Chen, Y.; Yan, G. Selective deposition of cocatalyst NiS on a g-C_3N_4/$ZnIn_2S_4$ heterojunction for exceptional photocatalytic H_2 evolution. New J. Chem. **2022**, 46. DOI: 10.1039/d2nj02545k.

31. Guan, Z.; Pan, J.; Li, Q.; Li, G.; Yang, J. Boosting Visible-Light Photocatalytic Hydrogen Evolution with an Efficient $CuInS_2$/$ZnIn_2S_4$ 2D/2D Heterojunction. ACS Sustainable Chem. Eng. **2019**, 7, 7736-7742. DOI: 10.1021/acssuschemeng.8b06587.